International Journal of Solids and Structures 51 (2014) 3350–3360

Contents lists available at ScienceDirect

International Journal of Solids and Structures

journal homepage: www.elsevier.com/locate/ijsolstr

A peridynamic implementation of crystal plasticity

S. Sun [1], V. Sundararaghavan *

University of Michigan, 1320 Beal Ave, 3025 FXB Building, Ann Arbor, MI 48109, USA

ARTICLE INFO

Article history:
Received 19 March 2014
Received in revised form 22 May 2014
Available online 19 June 2014

Keywords:
Microstructure
Crystal plasticity
Peridynamics
Simulation
Theory

ABSTRACT

This paper presents the first application of peridynamics theory for crystal plasticity simulations. A state-based theory of peridynamics is used (Silling et al., 2007) where the forces in the bonds between particles are computed from stress tensors obtained from crystal plasticity. The stress tensor at a particle, in turn, is computed from strains calculated by tracking the motion of surrounding particles. We have developed a quasi-static implementation of the peridynamics theory. The code employs an implicit iterative solution procedure similar to a non-linear finite element implementation. Peridynamics results are compared with crystal plasticity finite element (CPFE) analysis for the problem of plane strain compression of a planar polycrystal. The stress, strain field distribution and the texture formation predicted by CPFE and peridynamics were found to compare well. One particular feature of peridynamics is its ability to model fine shear bands that occur naturally in deforming polycrystalline aggregates. Peridynamics simulations are used to study the origin and evolution of these shear bands as a function of strain and slip geometry.

1. Introduction

Efficient micro-scale modeling tools are needed to compute microstructure-dependent properties of advanced structural alloys used in aerospace, naval and automotive applications. Integrated Computational Materials Engineering (ICME) (Allison et al., 2006) is an emerging paradigm that emphasizes integration of micro-scale material models with engineering analysis of products and processes so as to enable design of microstructurally tailored materials. One such model for metallic materials is based on finite element analysis of polycrystalline aggregates via crystal plasticity theory (Harren and Asaro, 1989; Bronkhorst et al., 1992; Becker and Panchanadeeswaran, 1995; Beaudoin et al., 1996; Sarma et al., 2002; Sundararaghavan and Zabaras, 2008). Here, mechanical properties of aggregates of grains are analyzed by discretizing the grains into finite elements and assigning crystallographic orientation to grains based on microdiffraction measurements (Qidwai et al., 2009). Deformation mechanisms are modeled using constitutive laws that consider crystallographic slip and reorientation of grains (texturing).

One particular drawback of standard finite element methods for crystal plasticity is observed during modeling of plastic localization zones. Such localization naturally occurs in deforming polycrystalline aggregates in the form of fine shear bands (Harren et al., 1988). The strains in these bands have been recently measured using micro-scale digital image correlation (DIC) (e.g. Kammers and Daly, 2013, see Fig. 1). In standard finite elements, the element size determines the size of shear bands (Anand and Kalidindi, 1994). Various enhancements of finite element method have been studied in the past to address the issue of mesh dependency. Early approaches involved development of traction-separation softening laws whose slope was made to depend on the element size (Oliver, 1989). In the limiting case of zero element size, the localization appears as a sharp discontinuity. Later approaches such as the extended finite element methods (X-FEM, Samaniego and Belytschko, 2005) or variational multiscale methods (VMM, Armero and Garikipati, 1996) directly represented discontinuities on coarse elements by enriching the finite element interpolations using fine-scale strain functions.

Another approach employs models that possess an intrinsic characteristic length scale. Examples of these ideas are non-local constitutive models (Bazant et al., 1984; Ghosh et al., 2013, 2014; Sundararaghavan and Waas, 2011), higher-gradient models (Coleman and Hodgdon, 1987) and more recently, peridynamic models (Silling, 2000). In peridynamics, the continuum domain is represented as a set of interacting particles. A state-based theory of peridynamics developed in Silling et al. (2007) formulates the forces between particles based on stress tensors obtained from continuum formulations (e.g. crystal plasticity). The stress tensor at a particle, in turn, is computed from strains calculated by tracking

* Corresponding author. Address: Associate Professor, Department of Aerospace Engineering. Tel.: +1 734 615 7242.
E-mail addresses: shangsun@umich.edu (S. Sun), veeras@umich.edu (V. Sundararaghavan).
[1] PhD Candidate, Department of Naval Architecture and Marine Engineering.

http://dx.doi.org/10.1016/j.ijsolstr.2014.05.027
0020-7683/

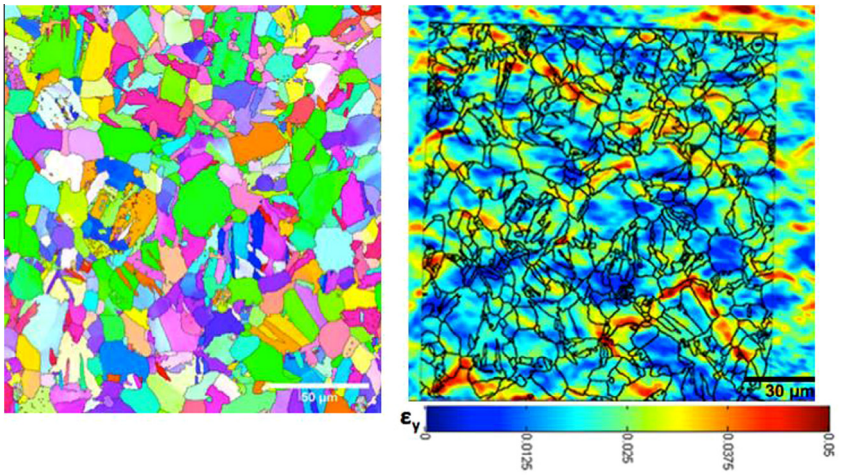

Fig. 1. Tensile strain field in a Titanium alloy microstructure as experimentally seen using micro-scale digital image correlation (Kammers and Daly, 2013, Prof. S. Daly, personal communication). Strains are seen to localize into shear bands within select grains.

the motion of surrounding particles. Using an integral form of the linear momentum balance equation, the method can directly model sharp displacement discontinuities (Agwai et al., 2011). This paper presents the first application of state-based peridynamic theory for crystal plasticity simulations. Current implementations of peridynamic state theory (Warren et al., 2009) employ explicit dynamic solution procedures that require small time steps for convergence. In this work, we employ a quasi-static implementation of the theory (Breitenfeld et al., 2014) and have extended it towards solving non-linear deformation problems. The solution procedure uses Newton–Raphson iterations similar to a non-linear finite element implementation. Thus, quasi-static peridynamics results can be quantitatively compared to conventional quasi-static crystal plasticity finite element simulations. Sections 2 and 3 of this paper provides the governing equations of the peridynamics theory and its numerical implementation. The crystal plasticity constitutive model is given in Section 4. In Section 5, we compare the method with crystal plasticity finite simulations and demonstrate the ability of peridynamics model to capture fine shear bands in grains. In the final section, conclusions and future work are discussed.

2. Peridynamics theory

In peridynamics theory, a material point $\boldsymbol{x}$ in the reference configuration $\mathcal{B}$ is assumed to interact with neighboring points $\boldsymbol{x}'$ (located within a finite radius δ) along a bond defined by the vector $\boldsymbol{x}'-\boldsymbol{x}$. The position of particle $\boldsymbol{x}$ in the current configuration is denoted by $\boldsymbol{y}=\boldsymbol{x}+\boldsymbol{u}_{\boldsymbol{x}}$, where $\boldsymbol{u}_{\boldsymbol{x}}$ denotes the displacement of particle $\boldsymbol{x}$. The kinematics of peridynamics theory is shown in Fig. 2.

The equation of balance of linear momentum at time t for the point $\boldsymbol{x}$ under quasi-static loading conditions is given by (Silling et al., 2007)

$$\begin{aligned}&\boldsymbol{L}(\boldsymbol{x})+\boldsymbol{b}(\boldsymbol{x})=0 \quad \forall x\in\mathcal{B},\\ &\boldsymbol{L}(\boldsymbol{x})=\int_{\mathcal{B}_x}\{\boldsymbol{T}[\boldsymbol{x}]\langle\boldsymbol{x}'-\boldsymbol{x}\rangle-\boldsymbol{T}[\boldsymbol{x}']\langle\boldsymbol{x}-\boldsymbol{x}'\rangle\}dV_{x'}\end{aligned} \tag{1}$$

where $\boldsymbol{b}$ is the body force, $\mathcal{B}_x$ is a spherical neighborhood of radius δ centered at $\boldsymbol{x}$ at time $t=0$. The term $\boldsymbol{T}[\boldsymbol{x}]\langle\boldsymbol{x}'-\boldsymbol{x}\rangle$ denotes the force (per unit volume squared) on material point $\boldsymbol{x}$ operating on the bond $\boldsymbol{x}'-\boldsymbol{x}$. The value of $\boldsymbol{T}$ can be obtained from the first Piola–Kirchhoff stress, $\boldsymbol{P}$, computed at point $\boldsymbol{x}$ from any conventional constitutive model (e.g. of the form $\boldsymbol{P}=\mathcal{F}(\boldsymbol{F})$, where $\boldsymbol{F}$ is the deformation gradient) as follows (Silling et al., 2007):

$$\boldsymbol{T}[\boldsymbol{x}]\langle\boldsymbol{x}'-\boldsymbol{x}\rangle=\omega\boldsymbol{P}\boldsymbol{K}^{-1}(\boldsymbol{x}'-\boldsymbol{x}) \tag{2}$$

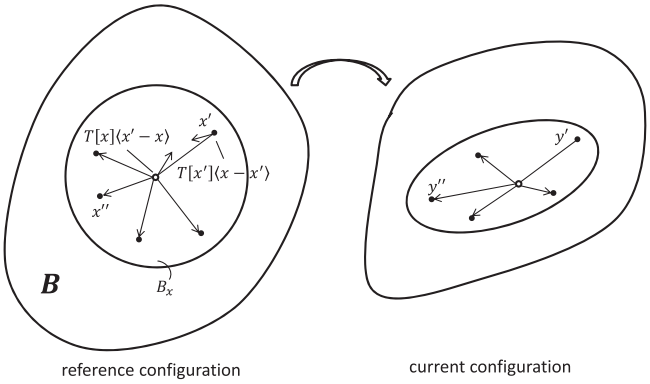

Fig. 2. Kinematics of peridynamics theory: Particle $\boldsymbol{x}$ is bonded to all particles within a region $\mathcal{B}_x$. Particle $\boldsymbol{x}$ maps to particle $\boldsymbol{y}$ in the deformed configuration. An averaged deformation gradient tensor can be defined that maps the bonds in the reference configuration to the deformed configuration. This quantity is used in the crystal plasticity constitutive model. The stresses obtained from the constitutive model can be mapped to bond force states $\boldsymbol{T}[\boldsymbol{x}]\langle\boldsymbol{x}'-\boldsymbol{x}\rangle$ in the reference configuration.

where, ω is an *influence function* defined at particle $\boldsymbol{x}$ which weights the contribution from each neighbor $\boldsymbol{x}'$ (for e.g. based upon the initial bond length $\omega=\hat{\omega}(|\boldsymbol{x}-\boldsymbol{x}'|)$) and $\boldsymbol{K}$ denotes a symmetric *shape tensor*, defined as

$$\boldsymbol{K}=\int_{\mathcal{B}_x}\omega(\boldsymbol{x}'-\boldsymbol{x})\otimes(\boldsymbol{x}'-\boldsymbol{x})dV_{x'} \tag{3}$$

The deformation gradient $\boldsymbol{F}$ (defined with respect to $\mathcal{B}$) at time t as needed in the constitutive models can be computed from the deformation of bonds attached to material point $\boldsymbol{x}$ as follows (Silling et al., 2007):

$$\boldsymbol{F}=\left(\int_{\mathcal{B}_x}\omega(\boldsymbol{y}'-\boldsymbol{y})\otimes(\boldsymbol{x}'-\boldsymbol{x})dV_{x'}\right)\boldsymbol{K}^{-1} \tag{4}$$

The derivation of Eqs. (2) and (4) can be found in Section 18 of Silling et al. (2007) where it is also shown that these definitions ensure the balance of angular momentum.

3. Numerical implementation

By dividing the body $\mathcal{B}$ into numbers of cells, each represented by a particle, the integral expressions can be rewritten as a

summation of discrete equations. For example, Eq. (1) is written as (neglecting body forces $\boldsymbol{b}$):

$$\boldsymbol{L}(\boldsymbol{x}) = \sum_{i=1}^{N} \{\boldsymbol{T}[\boldsymbol{x}]\langle \boldsymbol{x}'_i - \boldsymbol{x}\rangle - \boldsymbol{T}[\boldsymbol{x}'_i]\langle \boldsymbol{x} - \boldsymbol{x}'_i\rangle\}\Delta V_{x'_i} = 0 \tag{5}$$

where N is the number of the neighbor particles of material point $\boldsymbol{x}$ and the volume occupied by each particle is $\Delta V_{x'_i}$. To solve nonlinear equation $\boldsymbol{L}(\boldsymbol{x}) = \boldsymbol{0}$, a Newton Raphson iterative scheme is employed that solves for the increment in the particle displacements ($\delta \boldsymbol{u}_p$) using the following equation:

$$\mathcal{J}\delta \boldsymbol{u}_p = -\boldsymbol{L}(\boldsymbol{x}) \tag{6}$$

where, the right hand side is the residual vector and the Jacobian matrix $\mathcal{J} = \frac{\partial \boldsymbol{L}}{\partial \boldsymbol{u}_p}$ is defined implicitly by taking a derivative of Eq. (5) with respect to the vector of particle displacements:

$$d\boldsymbol{L}(\boldsymbol{x}) = \left[\sum_{i=1}^{N}\left(\frac{\partial \boldsymbol{T}[\boldsymbol{x}]\langle \boldsymbol{x}'_i - \boldsymbol{x}\rangle}{\partial \boldsymbol{u}_p} - \frac{\partial \boldsymbol{T}[\boldsymbol{x}'_i]\langle \boldsymbol{x} - \boldsymbol{x}'_i\rangle}{\partial \boldsymbol{u}_p}\right)\Delta V_{x'_i}\right]\delta \boldsymbol{u}_p = \mathcal{J}\delta \boldsymbol{u}_p \tag{7}$$

Using the tangent modulus $\frac{\partial \boldsymbol{P}}{\partial \boldsymbol{F}}$ obtained from a constitutive model (e.g. crystal plasticity), the derivative of $\boldsymbol{T}$ can be written using Eq. (2) as:

$$\frac{\partial \boldsymbol{T}[\boldsymbol{x}]\langle \boldsymbol{x}' - \boldsymbol{x}\rangle}{\partial \boldsymbol{u}_p} = \frac{\partial \boldsymbol{T}[\boldsymbol{x}]\langle \boldsymbol{x}' - \boldsymbol{x}\rangle}{\partial \boldsymbol{F}}\frac{\partial \boldsymbol{F}}{\partial \boldsymbol{u}_p} = \omega \frac{\partial \boldsymbol{P}}{\partial \boldsymbol{F}}\frac{\partial \boldsymbol{F}}{\partial \boldsymbol{u}_p}\boldsymbol{K}^{-1}(\boldsymbol{x}' - \boldsymbol{x}) \tag{8}$$

Using the above expression and the definition for $\boldsymbol{F}$ from Eq. (4), $d\boldsymbol{L}(\boldsymbol{x})$ can be written as follows:

$$\begin{aligned} d\boldsymbol{L}(\boldsymbol{x}) = \sum_{i=1}^{N}\Bigg[&\left(\omega_i \frac{\partial \boldsymbol{P}}{\partial \boldsymbol{F}}\left(\sum_{j=1}^{N}\omega_j(\delta \boldsymbol{u}_{x'_j} - \delta \boldsymbol{u}_x)\otimes(\boldsymbol{x}'_j - \boldsymbol{x})\boldsymbol{K}^{-1}\Delta V_{x'_j}\right)\right)\boldsymbol{K}^{-1}(\boldsymbol{x}'_i - \boldsymbol{x})\Delta V_{x'_i}\Bigg] \\ &- \sum_{i=1}^{N}\Bigg[\left(\omega'_i \frac{\partial \boldsymbol{P}'}{\partial \boldsymbol{F}'}\left(\sum_{j=1}^{N'}\omega'_j(\delta \boldsymbol{u}_{(x'_i)'_j} - \delta \boldsymbol{u}_{x'_i})\otimes((\boldsymbol{x}'_i)'_j - \boldsymbol{x}'_i)\boldsymbol{K}'^{-1}\Delta V_{(x'_i)'_j}\right)\right) \\ &\boldsymbol{K}'^{-1}(\boldsymbol{x} - \boldsymbol{x}'_i)\Delta V_{x'_i}\Bigg] \end{aligned} \tag{9}$$

The following notation is used in the above equation:

1. $\boldsymbol{x}'_i$ is the ith neighbor particle of $\boldsymbol{x}$,
2. $(\boldsymbol{x}'_i)'_j$ is the jth neighbor particle of $\boldsymbol{x}'_i$,
3. $\delta \boldsymbol{u}_{x'_j}$ is the displacement of particle $\boldsymbol{x}'_j$, etc.,
4. $N, K, \frac{\partial \boldsymbol{P}}{\partial \boldsymbol{F}}$ are the number of neighboring particles, the shape tensor and the tangent moduli, respectively, of particle $\boldsymbol{x}$; $N', K', \frac{\partial \boldsymbol{P}'}{\partial \boldsymbol{F}'}$ are the corresponding quantities for particle $\boldsymbol{x}'_i$,
5. ω_i and ω_j are the influence functions for the bonds $(\boldsymbol{x}'_i - \boldsymbol{x})$ and $(\boldsymbol{x}'_j - \boldsymbol{x})$ respectively; ω'_i and ω'_j are defined for bonds $(\boldsymbol{x} - \boldsymbol{x}'_i)$ and $((\boldsymbol{x}'_i)'_j - \boldsymbol{x}'_i)$.

The above equation for $d\boldsymbol{L}(\boldsymbol{x})$ leads to an implicit form for the Jacobian $\mathcal{J}$ for use in Eq. (6). For a 2D problem, the global matrix is $2N_{total} \times 2N_{total}$ where N_{total} is the total number of particles in the simulation. The sparseness of the matrix depends on the radius of influence δ, and varies from sparsely populated for a small cutoff that only includes nearest neighbor interactions (Fig. 3) to a fully populated matrix for a large cutoff (a highly non-local system). The system of equations are iteratively solved until $||\delta \boldsymbol{u}_p|| < \epsilon_1$, where $\epsilon_1 = 10^{-6}$, a small numerical cut-off. The crystal plasticity formulation uses displacement boundary conditions that are directly enforced on the boundary particles ($\boldsymbol{u}_x = (\exp(\boldsymbol{L}_{macro}t) - \boldsymbol{I})\boldsymbol{x}$) (Sundararaghavan and Zabaras, 2006) based on a macroscopic velocity gradient $\boldsymbol{L}_{macro} = \dot{\boldsymbol{F}}\boldsymbol{F}^{-1}$, time t and identity matrix $\boldsymbol{I}$. [2] After solving the system, the inner particle displacements are incremented by $\delta \boldsymbol{u}_p$. The history-dependent variables in the constitutive equations are then updated for use in the next loading step. The constitutive model is described next.

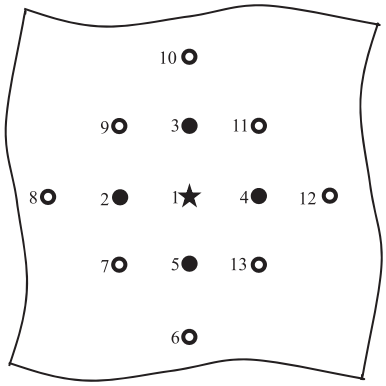

Fig. 3. Illustration of one particle interaction for a peridynamics model with nearest neighbor interactions. Here, particles $i = 2, 3, 4, 5$ (denoted as $\boldsymbol{x}'_i$) are neighbors of the particle 1 (denoted as $\boldsymbol{x}$). Particles $j = 1, 7, 8, 9$ (denoted as $(\boldsymbol{x}'_2)'_j$) represent the neighbors of particle 2 ($\boldsymbol{x}'_2$). In this case, the row of Jacobian $\mathcal{J}$ corresponding to particle 1 will include entries from all 13 particles shown here.

4. Crystal plasticity constitutive model

Single-crystal plasticity theory (Anand and Kothari, 1996) will be used to model deformation response of particles within each grain. The theory is based on the notion that plastic flow takes place through slip on prescribed slip systems. For a material with $\alpha = 1, \ldots, N$ slip systems defined by ortho-normal vector pairs $(\boldsymbol{m}_0^\alpha, \boldsymbol{n}_0^\alpha)$ denoting the slip direction and slip plane normal respectively at time $t = 0$, the constitutive equations relate the following basic fields (all quantities expressed in crystal lattice coordinate frame): the deformation gradient $\boldsymbol{F}$ defined with respect to the initial undeformed crystal which can be decomposed into elastic and plastic parts as $\boldsymbol{F} = \boldsymbol{F}^e\boldsymbol{F}^p$ (with $\det(\boldsymbol{F}^p) = 1$), the Cauchy stress $\boldsymbol{\sigma}$ and the slip resistances $s^\alpha > 0$. In the constitutive equations to be defined below, the Green elastic strain measure $\bar{\boldsymbol{E}}^e = \frac{1}{2}\left(\boldsymbol{F}^{e^T}\boldsymbol{F}^e - \boldsymbol{I}\right)$ defined on the relaxed configuration (plastically deformed, unstressed configuration $\bar{\mathcal{B}}$) is utilized. The conjugate stress measure is then defined as $\bar{\boldsymbol{T}} = \det\boldsymbol{F}^e(\boldsymbol{F}^e)^{-1}\boldsymbol{\sigma}(\boldsymbol{F}^e)^{-T}$. Kinematics of single crystal slip is illustrated in Fig. 4.

The constitutive relation, for stress, is given by $\bar{\boldsymbol{T}} = \mathcal{L}^e[\bar{\boldsymbol{E}}^e]$ where $\mathcal{L}^e$ is the fourth-order anisotropic elasticity tensor. It is assumed that deformation takes place through dislocation glide and the evolution of the plastic velocity gradient is given by:

$$\boldsymbol{L}^p = \dot{\boldsymbol{F}}^p(\boldsymbol{F}^p)^{-1} = \sum_\alpha \dot{\gamma}^\alpha \boldsymbol{S}_0^\alpha sign(\tau^\alpha) \tag{10}$$

where $\boldsymbol{S}_0^\alpha = \boldsymbol{m}_0^\alpha \otimes \boldsymbol{n}_0^\alpha$ is the Schmid tensor and $\dot{\gamma}^\alpha$ is the plastic shearing rate on the αth slip system. The resolved stress on the αth slip system is given by $\tau^\alpha = \bar{\boldsymbol{T}} \cdot \boldsymbol{S}_0^\alpha$.

A rate independent algorithm is employed to solve the single crystal model. The resolved shear stress τ^α is taken to attain a critical value s^α (the slip system resistance) on the systems where slip occurs. These active systems have a plastic shearing rate $\dot{\gamma}^\alpha > 0$. There is no plastic shearing rate ($\dot{\gamma}^\alpha = 0$) on inactive slip systems where the resolved shear stress does not exceed s^α. The evolution of slip system resistance given by the following expression:

$$\dot{s}^\alpha(t) = \sum_\beta h^{\alpha\beta}\dot{\gamma}^\beta(t), \quad \text{with} \quad s^\alpha(0) = \tau_0^\alpha \tag{11}$$

[2] Recent work has shown that zero-energy modes are inherent in the state-based theory of peridynamics and various measures to mitigate this effect are listed in Breitenfeld et al. (2014). From our simulations, we see that the use of displacement constraints on all boundaries suppresses zero-energy modes at moderate strain levels.

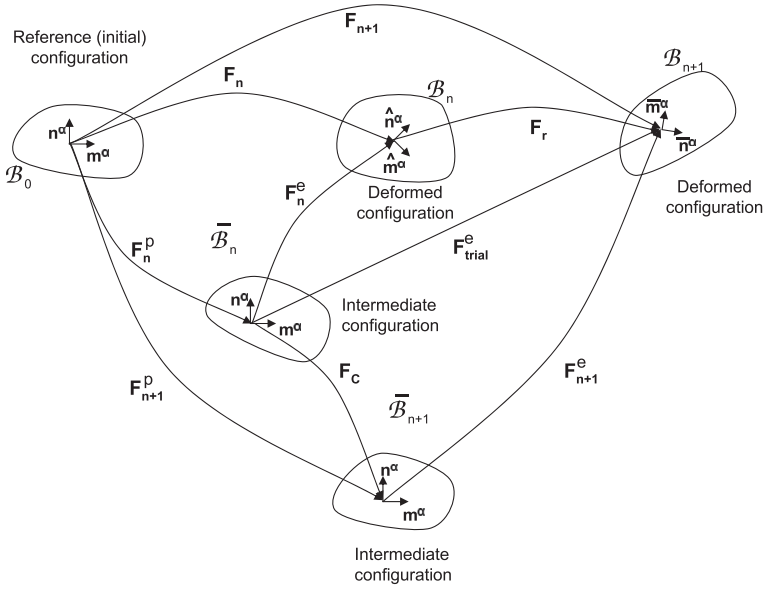

Fig. 4. Schematic of the various material configurations, for a single crystal, used in the integration of the constitutive model. The slip systems ($\boldsymbol{m}^\alpha, \boldsymbol{n}^\alpha$ are known on the reference (initial) configuration. Also, $\hat{\boldsymbol{m}}^\alpha$, $\bar{\boldsymbol{m}}^\alpha$ are the slip directions (different from $\boldsymbol{m}^\alpha$ because of crystal re-orientation) in the deformed configurations $\mathcal{B}_n$ and $\mathcal{B}_{n+1}$, respectively.

Here, $h^{\alpha\beta}$ is the slip system hardening term, $\dot{\gamma}^\beta$ is the plastic shearing rate on the βth slip system, and τ_0^α is the initial slip system resistance on the αth slip system.

The algorithm for computing the plastic shear increment $\Delta\gamma^\beta$ from this model be found in the appendix A. Subsequently, the plastic part of the deformation gradient is updated using Eq. (10), the elastic part computed from $\boldsymbol{F} = \boldsymbol{F}^e\boldsymbol{F}^p$. The conjugate stress measure, $\bar{\boldsymbol{T}}$ is then computed from $\bar{\boldsymbol{T}} = \mathcal{L}^e[\bar{\boldsymbol{E}}^e]$ and converted to the Piola–Kirchhoff-I stress, $\boldsymbol{P} = (\det\boldsymbol{F})\boldsymbol{\sigma}\boldsymbol{F}^{-T}$ for use in Eq. (2). The slip resistances are also updated at the end of the time step using Eq. (11). Finally, the tangent modulus $\frac{\partial \boldsymbol{P}}{\partial \boldsymbol{F}}$ for use in Eq. (9) is computed using a fully implicit algorithm described in Appendix B.

5. Numerical examples: peridynamic crystal plasticity

We consider planar polycrystals characterized by a two dimensional rotation $\boldsymbol{R}$ that relates the local crystal lattice frame to the reference sample frame. A parametrization of the associated rotation group is,

$$\boldsymbol{R} = \boldsymbol{I}\,cos(g) - \boldsymbol{E}\,sin(g) \tag{12}$$

where g is the angle between the crystal and sample axes, $\boldsymbol{E}$ is the two dimensional alternator ($E_{11} = E_{22} = 0, E_{12} = -E_{21} = 1$), and $\boldsymbol{I}$ is the identity tensor. A general planar crystal with symmetry under rotations through π is considered here. Under the symmetry, crystal orientations can be described uniquely by parameters drawn from a simply connected fundamental region $(-\pi/2, \pi/2)$. Due to symmetry, the orientation $\pi/2$ is exactly the same as orientation $-\pi/2$. During the peridynamics simulation, the crystal reorientation velocity ($\boldsymbol{v} = \frac{\partial \boldsymbol{g}}{\partial t}$) is obtained by taking a derivative of relation Eq. (12):

$$\boldsymbol{v} = \frac{1}{2}E.\Omega \tag{13}$$

where $\boldsymbol{\Omega}$ is the spin tensor defined as $\boldsymbol{\Omega} = \dot{\boldsymbol{R}}^e\boldsymbol{R}^{eT}$. Here, $\boldsymbol{R}^e$ is evaluated through the polar decomposition of the elastic deformation gradient $\boldsymbol{F}^e$ as $\boldsymbol{F}^e = \boldsymbol{R}^e\boldsymbol{U}^e$. The texturing of the polycrystal is tracked by computing the change in orientation $\Delta\boldsymbol{g} = \boldsymbol{v}\Delta t$ of particles at each time step.

A 1×1 mm^2 microstructure with a total of 19 grains was computationally generated using Voronoi construction as shown in Fig. 5(a). The microstructure is subjected to plane strain compression with the imposed macroscopic velocity gradient $\boldsymbol{L}$ given as:

$$\boldsymbol{L} = \eta\begin{bmatrix} 1 & 0 \\ 0 & -1 \end{bmatrix} \tag{14}$$

where η is a constant strain rate, taken to be 0.0020. The simulations were performed over 30 steps with this velocity gradient, leading to a final strain of about 0.06.

Twelve different orientations from within the interval $(-\pi/2, \pi/2)$ (step size of $\pi/12$) were distributed among the grains. Two slip systems at orientations $-\pi/6$ and $+\pi/6$ were considered. The values in the elastic stiffness matrix are taken as $\mathbb{C}_{11} = 2$ GPa and $\mathbb{C}_{12} = \mathbb{C}_{44} = 1$ GPa. The particular hardening law (Anand and Kothari, 1996) in Eq. (11) was chosen as follows:

$$h^{\alpha\beta} = h_o^\beta(q + (1-q)\delta^{\alpha\beta})\left(1 - \frac{s^\beta(t)}{s_s^\beta}\right)^a \text{(no sum on } \beta) \tag{15}$$

The slip system hardening term ($h^{\alpha\beta}$) includes latent hardening through parameter q. In this term, h_o^β is the hardening coefficient and s_s^β is the saturation resistance of slip system β. The values for the slip hardening parameters are taken to be identical for both slip systems and are listed below:

$$h_o = 10\text{ MPa}, \quad s_s = 200\text{ MPa}, \quad a = 2, \quad \tau_0 = 10\text{ MPa}, \quad q = 1.4 \tag{16}$$

h_o is the hardening constant, s_s is the saturation value of slip system resistance, τ_0 is the initial slip system resistance, q is the latent hardening parameter and a is the exponent in the hardening law (Eq. (15)). Results from the peristatic model are compared with a crystal plasticity finite element (CPFE) model (from Sun and Sundararaghavan, 2012). The CPFE model in Sun and Sundararaghavan (2012) also contained the Hall–Petch terms to model the effect of grain size on the plastic response, the code was modified to use the simplified hardening law (Eq. (15)) from Anand and Kothari (1996).

While the underlying constitutive equations for both peristatic and CPFE models are the same, differences emerge from the governing equation (linear momentum conservation). The governing

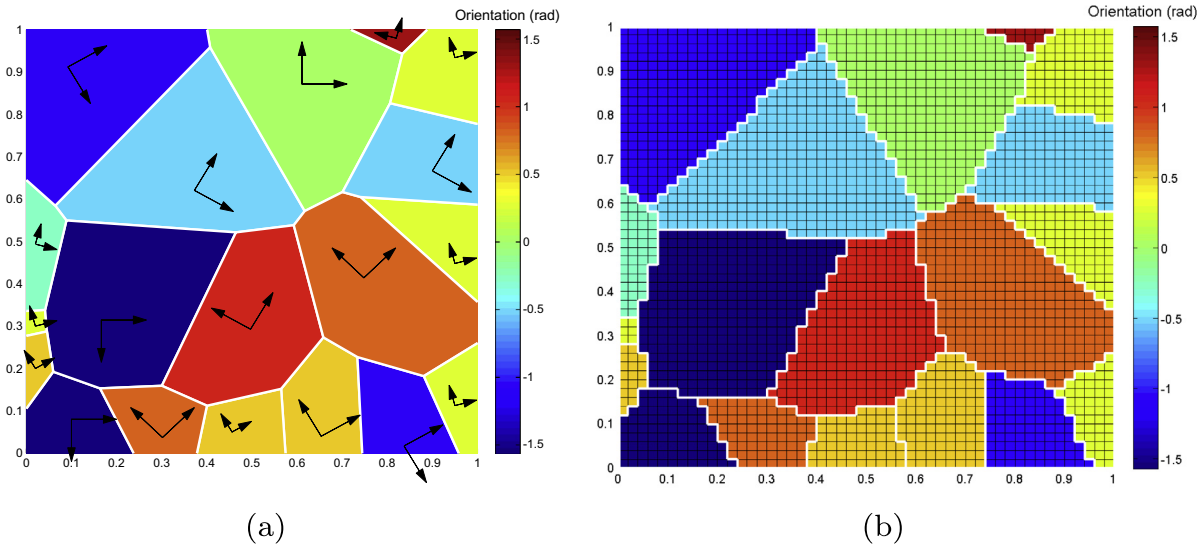

Fig. 5. (a) Initial microstructure represented by 19 planar grains with the crystal coordinate system indicated (b) Pixel-based grid is used to represent the microstructure in finite element calculations.

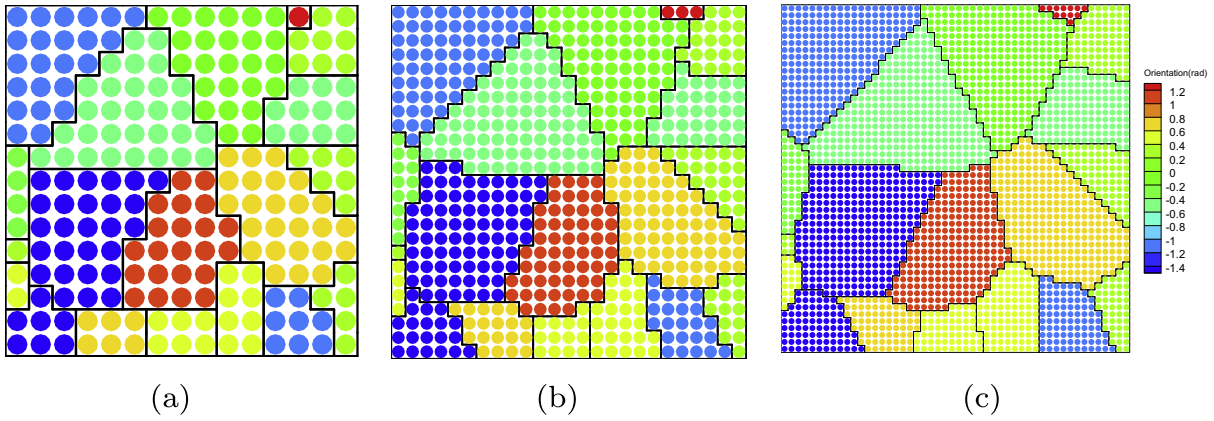

Fig. 6. Particle grids employed in this work, the particles are located at the centers of elements in pixel-based grids (a) 225 particles (b) 625 particles (c) 2500 particles.

equations for peridynamics theory is of the non-local (integral) form that includes long range interactions while the corresponding CPFE equations are (differential) form. A quantitative comparison of these theories can be enabled if the non-locality of the peristatic theory is kept to a minimum by using the lowest possible radius of interaction for the particles, and using similar meshes. This involves including just the nearest neighbor interactions by bonding of each particle to its four nearest neighbors similar to an Ising model (Ising, 1925).[3] The influence function ω was taken to be a constant ($\omega = 1$) to circumvent the issue of fitting an influence function (Silling et al., 2007). The finite element mesh used the same number of elements as the number of particles in the peristatic case. The model is discretized using a peridynamics case. The model is discretized using a pixel mesh (four noded square elements) as shown in Fig. 5(b). The particles in the peristatic simulations were located at the center of these elements. Each particle occupies a constant volume in the reference configuration equal to the area of the enclosing finite element. Three cases were considered with 225, 625 and 2500 particles, respectively, as shown in Fig. 6.

The particles in the peridynamics simulation are colored using field values in order to compare with finite element contours obtained from the CPFE model. The same contour levels were used and the figures are best compared in color (in the electronic version of the manuscript). In Fig. 7, the x-stress σ_{xx} contours of peridynamics and CPFE model are compared at the final strain. Results for a 225 element and a 625 element simulation are shown. Although the overall stress distribution and the locations of maximum and minimum stresses are similar between these two models, certain differences are seen that become more pronounced at a higher mesh refinement. For example, Fig. 8 shows the comparison of the x-stress contours for a 2500 element mesh. The differences seen pertain to the emergence of shear bands in the microstructure. Although the locations and orientations of shear bands are identical, the bands seen from FE simulations are comparatively more diffuse. As an example, the width of a shear band at the same location in both models are shown using lines superposed on a grain in Fig. 8. Two key differences are seen when comparing the two models. Firstly, FE results show thicker shear bands that can be attributed to lack of an internal length scale; an issue that is well studied in literature (e.g. Samaniego and Belytschko, 2005). Peridynamic models do include an explicit length scale in the form of a radius of interaction and lead to finer shear bands,

[3] Note that the non-locality of peristatic theory implies that there is an implicit interaction of field quantities over 13 particles (as illustrated in Fig. 3).

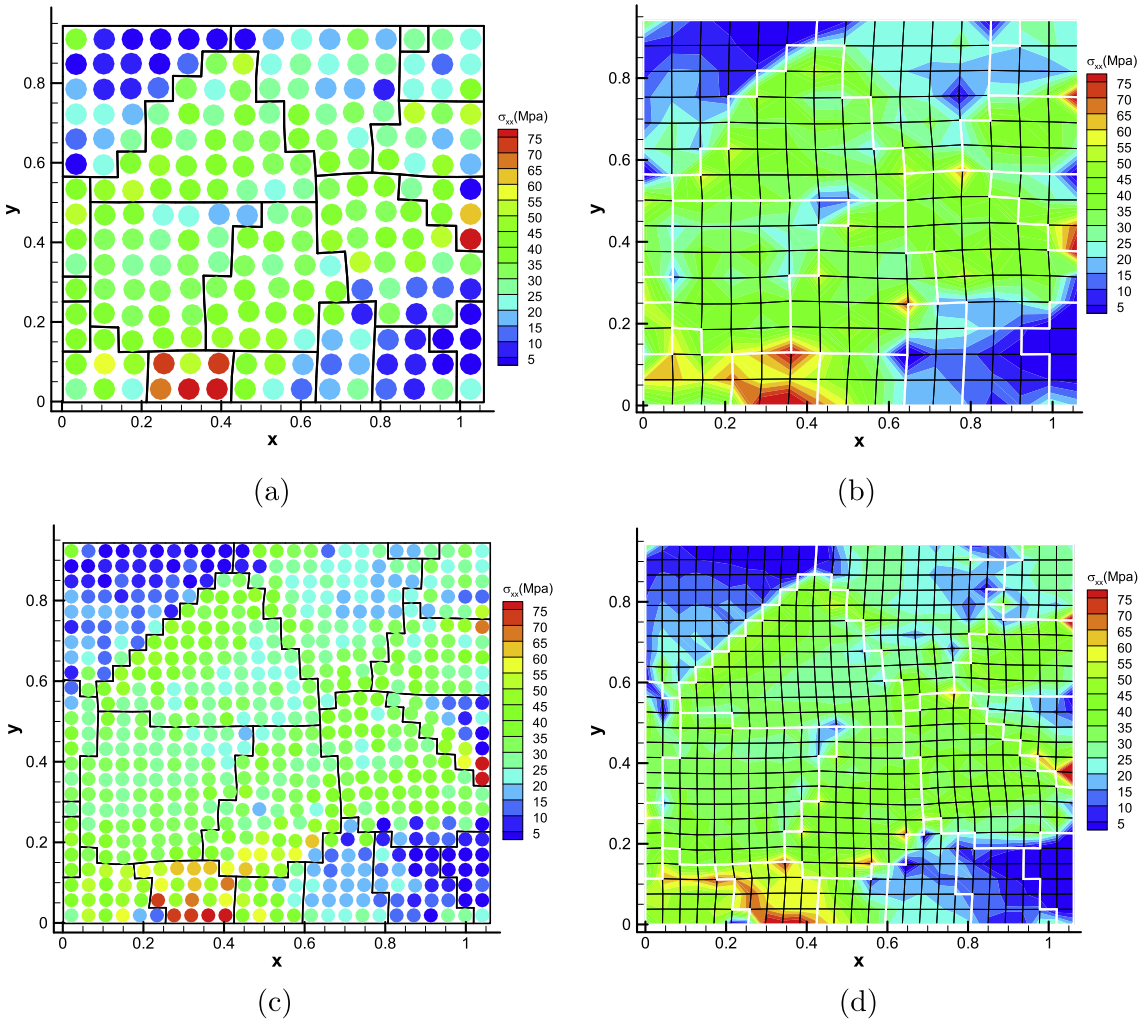

Fig. 7. Comparison of σ_{xx} from peridynamics and CPFE model for a 225 particle/element mesh in (a,b) and a 625 element mesh in (c,d).

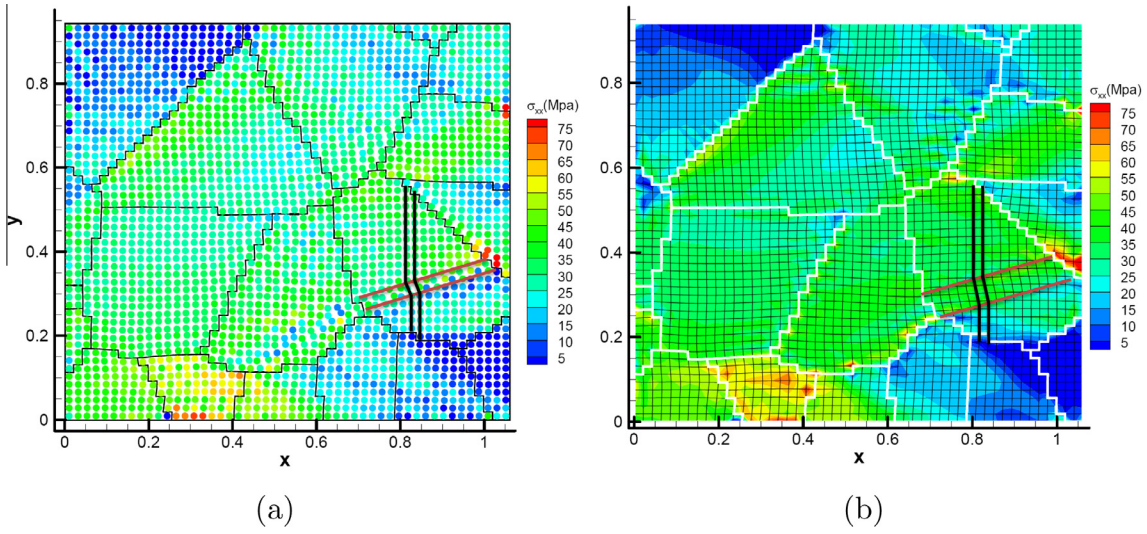

Fig. 8. Comparison of σ_{xx} between peridynamics and FE results (a) 2500 particle peridynamics (b) 2500 element CPFE model. The width of a shear band is compared.

qualitatively closer to those seen in experiments (Dmitrieva et al., 2009). Secondly, the nature of shearing within the band is heterogeneous in the peridynamics case; as seen from the irregular positions of within the shear band in a peristatic case versus a more uniform distribution of shear strain across the band in the CPFE case. Such inhomogeneities within a shear band have also

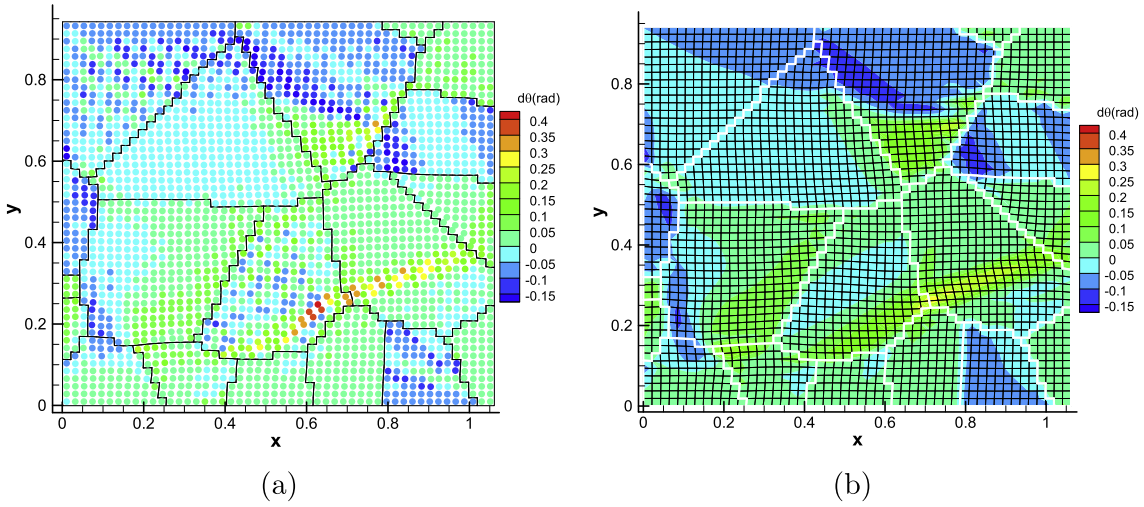

Fig. 9. (a) Orientation change for 2500 particles from peridynamics (b) CPFE result.

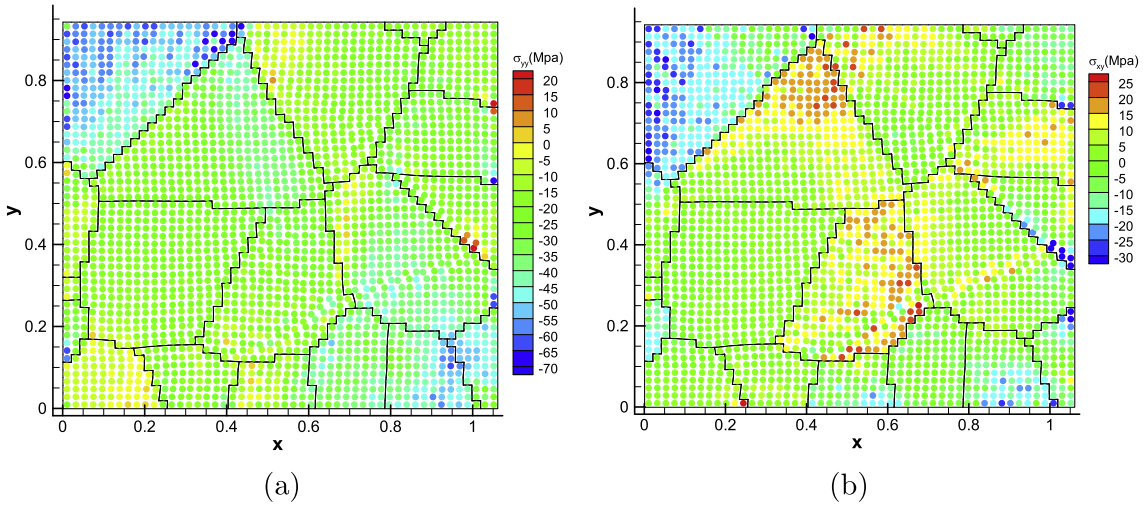

Fig. 10. Comparison of components of stress tensor from peridynamics simulation (a) σ_{yy} (b) σ_{xy}.

been measured experimentally (EBSD results from Dmitrieva et al., 2009) in the Dmitrieva et al. (2009)) in the form of (almost periodic) changes in orientation within a shear band.

To test this aspect, the reorientation map predicted by the peridynamics and CPFE models are compared in Fig. overall contours predicted by CPFE and peristatic models are similar. Significant reorientation is seen within shear bands in both models, although the CPFE results are more diffuse and weaker in intensity compared to the peristatic simulation. Interestingly, the orientation changes within the shear band indicated in Fig. 8 show periodic behavior seen from recent experiments (Dmitrieva et al., 2009). Other components of the stress tensor (y-stress and xy-shear stress) predicted by peridynamics are shown in Fig. 10. These stresses display localization in regions that are different from those seen in the x-stress contours. For example, the grain with the shear band indicated in Fig. 8 also has a band of high y- and xy- stresses lying along the grain boundary to the left, adjacent to a grain with high shear stresses. The shear band indicated in Fig. 8 extends into the grain to the left, and this band is seen to have lower shear stresses compared to the surrounding grain.

The origin of shear bands is studied next through analysis of time evolution of the microstructure during loading. Firstly, the potential active slip systems were identified using a rudimentary Schmid factor analysis. To compute the maximum Schmid factor for each grain, the loading axis is represented in the crystal frame of reference as $v_c = \boldsymbol{R}^T v_s$ where v_s is the loading axis in the sample reference frame (here, $v_s = [1;0]$). The Schmid factor for each slip system was identified as $\mathbb{S}^\alpha = |(m_0^{\alpha^T} * v_c)(n_0^{\alpha^T} * v_c)|$ and the slip system with the maximum Schmid factor was marked as the active system. Fig. 11(a) shows a plot of the maximum Schmid factor in each grain. Each grain is marked with the slip system number (α) that gives the maximum Schmid factor. If the Schmid factor for both slip systems are equal within a grain, both the systems are marked. The equivalent plastic strain increment[4] at an effective strain of 0.02 is shown in Fig. 11(b). A comparison of these two figures (Fig. 11(a) and (b)) shows that the deformation processes primarily occur in grains with a high Schmid factor. Little plasticity, if any, is seen in the grains with the lowest Schmid factor. The plastic shearing increments ($\Delta\gamma^1$ and $\Delta\gamma^2$) on slip systems 1 and 2 are shown in Fig. 11(c) and (d) respectively at an effective strain of

[4] The equivalent plastic strain increment is defined as (Anand and Kalidindi, 1994) $d\epsilon^p = \frac{\sum_\alpha \tau^\alpha \Delta\gamma^\alpha}{\sigma_{eff}}$ where, σ_{eff} is the von Mises stress.

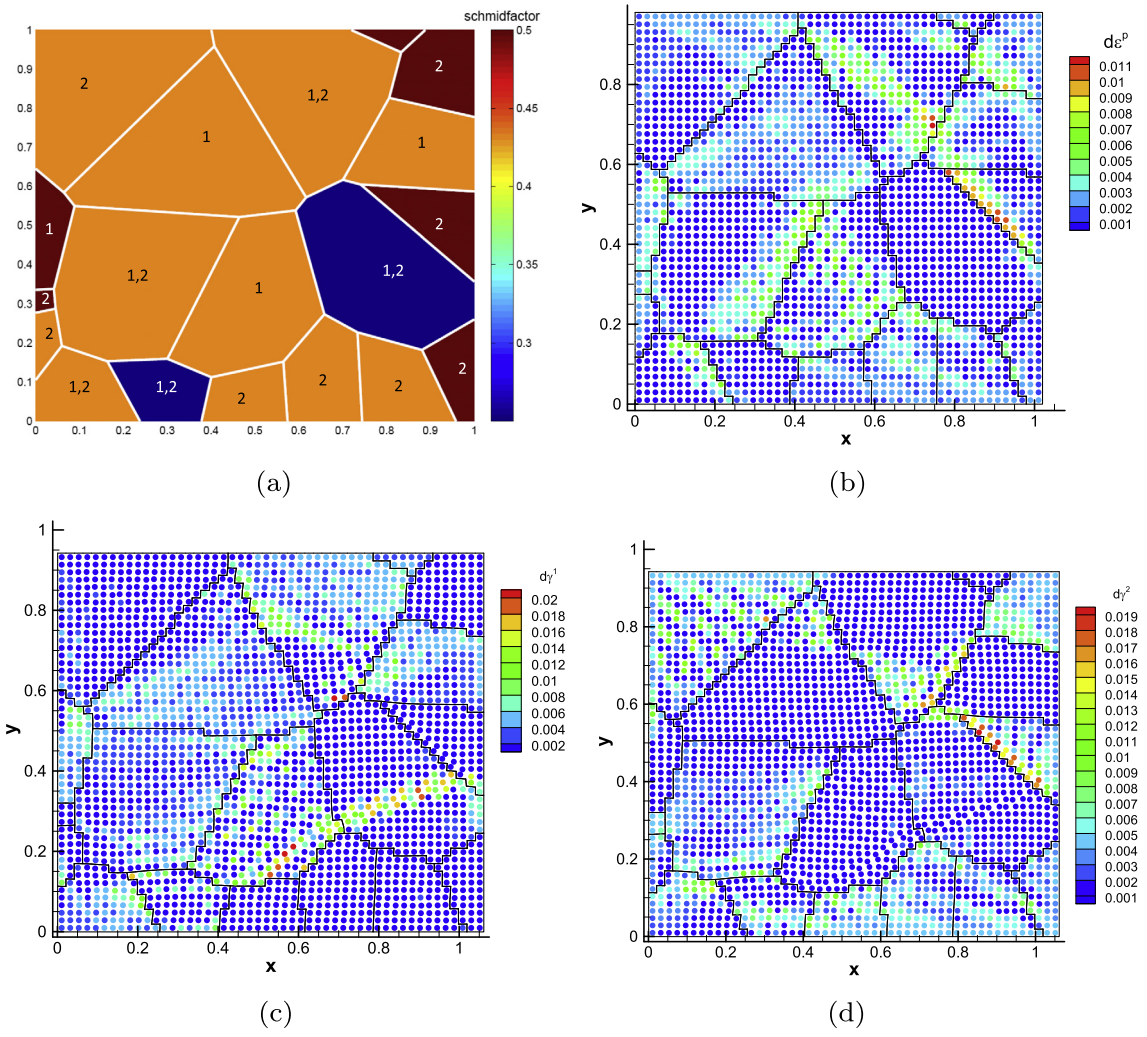

Fig. 11. (a) Maximum Schmid factors of grains, the slip system corresponding the maximum Schmid factor is marked on the grains (b) Contours of equivalent plastic strain increment at low strains ($\epsilon = 0.02$) show no slip activity on grains with the lowest Schmid factor (c) Plastic shear increments for slip system 1 (largely occur on grains marked '1' in the Schmid factor plot). (d) Plastic shear increments of slip system 2 (largely occur on grains marked '2' in the Schmid factor plot).

0.06. The shear increments for slip system 1 shown in Fig. 11(c) largely occur on grains marked '1' in Fig. 11(a). Similarly, the shear increments of slip system 2 shown in Fig. 11(d) largely occur on grains marked '2' in Fig. 11(a). On grains where both slip systems have the same Schmid factor, the grain is seen to be partitioned into sections where one of the two slip systems are active. As seen previously in Fig. 9, these grain sections have different reorientation angles that eventually partition the grain into two or more orientations. Interestingly, shear bands become active in low Schmid factor grains at larger strains (e.g. the grain marked in Fig. 8 was a low Schmid factor grain), indicating that this is a possible deformation mechanism in grains that are not favorably oriented for slip activity. Finally, the shear increments are seen to form a laminated pattern in several grains. The evolution of this lamellae and shear bands were studied as a function of strain to identify relationships, if any, between these features and the slip geometry.

Fig. 12(a) shows the orientation of active slip systems for each grain as identified using the Schmid factor analysis. The evolution of the effective plastic strain increments are shown in Fig. 12(b)–(d) as a function of increasing applied strain. We see that the shear band (in the grain shown in Fig. 8) does not form along any particular slip direction. As the microstructure is loaded, strain localization progresses in the form of a laminated pattern. While some lamellae do bear a relationship with slip direction, in general, lamellae appear to align with directions along which shear bands eventually form. Recent experiments (based on digital image correlation, Zhu et al., 2012) also indicate that shear banding initiates in the form of lamellae of localized strain that eventually merge to form a larger shear band. These shear bands move into neighboring grains and the process repeats through formation of new lamellar structures.

Finally, a comparison of simulation times for the CPFE and peridynamic models is shown for different mesh sizes in Fig. 13. Both CPFE and peridynamics simulations are fully parallel and utilize eight (3 GHz) processors on a HP workstation. The simulation times were computed based on the first ten time steps ($\Delta t = 0.1$ s) of each method and normalized with respect to the simulation time for the most expensive approach. CPFE was the more expensive approach for all three meshes. This is primarily due to the fact that FE simulations employ four integration points per element, which increases both the number of calculations and quadruples the amount of storage (of constitutive model parameters such as elastic and plastic deformation gradients) versus a peristatic case. On the other hand, peristatic model does have a less sparse global matrix and thus, the solution time is comparatively higher. However, for the nearest neighbor interactions modeled

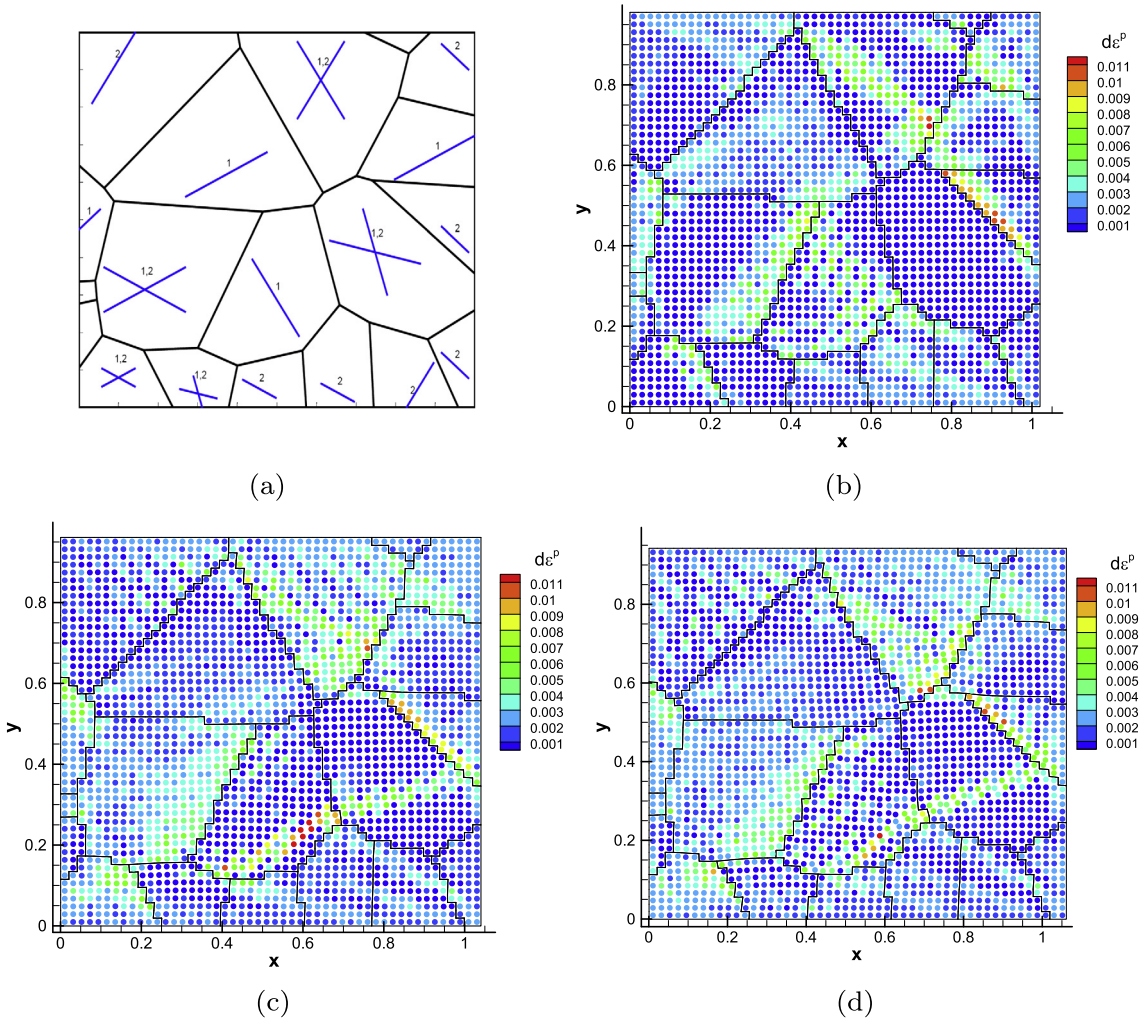

Fig. 12. (a) Active slip systems identified using a simple Schmid factor analysis (b) Contours of equivalent plastic strain increment at $\epsilon = 0.02$ (c) Contours at $\epsilon = 0.04$ (d) Contours at $\epsilon = 0.06$.

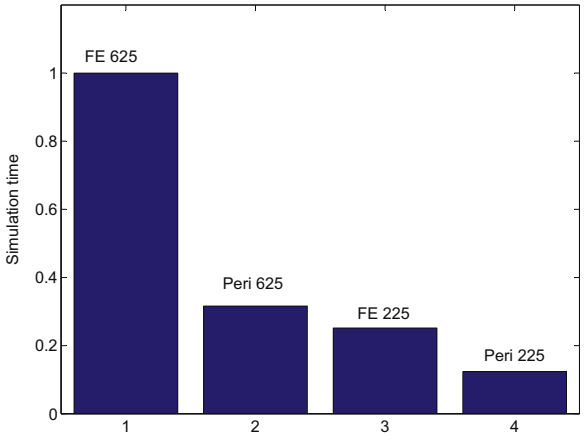

Fig. 13. Comparison of simulation times (normalized) for two methods.

in this work, the sparseness issue did not seem to increase the computational time as much. We expect both the assembly and solution time to increase significantly with increase in the radius of influence (δ) making FE simulations faster when including longer range interactions.

6. Conclusions and future work

The primary contribution of this work is a fully implicit numerical implementation of crystal plasticity within a peridynamics framework. A state-based theory of peridynamics is used (Silling et al., 2007) where the bond forces are described using second-order stress tensors computed using a standard crystal plasticity constitutive model. The deformation gradient at the particle is computed using the motion of the collection of particles within a radius of influence. The highlight of this approach is that the model is fully non-local, without the need to make any change to the underlying constitutive model. A Newton–Raphson implementation of peridynamics is developed here that allows solution of a general non-linear, finite deformation crystal plasticity problem. The peridynamics results were compared against crystal plasticity finite element (CPFE) analysis for the problem of plane strain compression of a planar polycrystal. The stress, strain and texture fields predicted by CPFE and peridynamics were found to be largely similar. One particular feature of peridynamics is its ability to model fine shear bands that occur naturally in deforming polycrystalline aggregates. The particles within a shear band show inhomogeneity in plastic deformation and reorientation. Peridynamics simulations were used to study the origin and evolution of these shear bands as a function of strain and slip geometry. It is seen that the shear band formation is a favorable deformation mode in grains with a low

Schmid factor. Shear bands are found to originate in the form of lamellar structures that merge to form a single shear band. The orientation of the shear band, by itself, are not aligned with the slip directions. Future work will be focused on extending the formulation to study 3D crystal structures (e.g. FCC Aluminum) and quantitative validation through comparison to in situ micro-DIC experiments. We also plan to perform a parametric study of the effect of misorientation distribution, crystal structure and deformation on the activation and propagation of shear bands.

Acknowledgements

The work presented here was funded by Office of Naval Research (ONR) grant N00014-12-1-0013 and National Science Foundation CAREER award (CMMI-0954390).

Appendix A

A.1. Constitutive update scheme

The quantities at the current time step are denoted by subscript $(n+1)$. The deformation gradient $\boldsymbol{F}_{n+1}$ is known at the current time step and the update procedure given here is used to compute the PK-I stress $\boldsymbol{P}=\mathcal{F}(\boldsymbol{F}_{n+1})$ where $\mathcal{F}$ is the constitutive model described in Section 4.

An Euler-backward time integration procedure for Eq. (10) leads to the following approximation:

$$\boldsymbol{F}^p=\exp\left(\Delta t\sum_\alpha \dot{\gamma}^\alpha \boldsymbol{S}_0^\alpha sign(\tau^\alpha)\right)\boldsymbol{F}_n^p \approx \left(\boldsymbol{I}+\sum_\alpha \Delta\gamma^\alpha \boldsymbol{S}_0^\alpha sign(\tau^\alpha)\right)\boldsymbol{F}_n^p \tag{17}$$

Substituting Eq. (17) into the multiplicative decomposition $\boldsymbol{F}=\boldsymbol{F}^e\boldsymbol{F}^p$ results in the following:

$$\boldsymbol{F}^e=\boldsymbol{F}^e_{trial}\left(\boldsymbol{I}-\sum_\alpha \Delta\gamma^\alpha \boldsymbol{S}_0^\alpha sign(\tau^\alpha)\right) \tag{18}$$

where $\boldsymbol{F}^e_{trial}$ is the trial elastic deformation gradient and is given as $\boldsymbol{F}_{n+1}(\boldsymbol{F}_n^p)^{-1}$.

The Green elastic strain measure is computed using Eq. (18) as

$$\bar{\boldsymbol{E}}^e=\frac{1}{2}\left(\boldsymbol{F}^{eT}\boldsymbol{F}^e-\boldsymbol{I}\right)=\bar{\boldsymbol{E}}^e_{trial}-\frac{1}{2}\sum_\alpha sign(\tau^\alpha)\Delta\gamma^\alpha \boldsymbol{B}^\alpha \tag{19}$$

where $\bar{\boldsymbol{E}}^e_{trial}$ and $\boldsymbol{B}^\alpha$ are defined as

$$\begin{aligned}\bar{\boldsymbol{E}}^e_{trial}&=\frac{1}{2}\left((\boldsymbol{F}^e_{trial})^T\boldsymbol{F}^e_{trial}-\boldsymbol{I}\right)\\ \boldsymbol{B}^\alpha&=(\boldsymbol{S}_0^\alpha)^T(\boldsymbol{F}^e_{trial})^T\boldsymbol{F}^e_{trial}+(\boldsymbol{F}^e_{trial})^T\boldsymbol{F}^e_{trial}\boldsymbol{S}_0^\alpha\end{aligned} \tag{20}$$

Using Eq. (19) in the constitutive relation for stress $\bar{\boldsymbol{T}}=\mathcal{L}^e[\bar{\boldsymbol{E}}^e]$ leads to the following

$$\bar{\boldsymbol{T}}=\bar{\boldsymbol{T}}_{trial}-\frac{1}{2}\sum_\beta \Delta\gamma^\beta \mathcal{L}^e\left[\boldsymbol{B}^\beta\right]sign(\boldsymbol{\tau}^\beta_{trial}) \tag{21}$$

where $\bar{\boldsymbol{T}}_{trial}=\mathcal{L}^e[\bar{\boldsymbol{E}}^e_{trial}]$.

A trial resolved shear stress $\boldsymbol{\tau}^\alpha_{trial}=\bar{\boldsymbol{T}}_{trial}\cdot\boldsymbol{S}_0^\alpha$ is then computed. A potentially active set $\mathcal{PA}$ of slip systems can be identified based on the trial resolved stress as the systems with $|\boldsymbol{\tau}^\alpha_{trial}|-s^\alpha>0$.

During plastic flow, the active systems are assumed to follow the consistency condition: $|\tau^\alpha|=s^\alpha$. Increment in shearing rates $\Delta\gamma^\beta$ at each time step is obtained by solving the following equation obtained by resolving Eq. (21) along slip directions:

$$|\tau^\alpha|=s^\alpha=|\tau^\alpha_{trial}|-\frac{1}{2}\sum_\beta sign(\tau^\alpha_{trial})sign(\tau^\beta_{trial})\Delta\gamma^\beta\mathcal{L}^e\left[\boldsymbol{B}^\beta\right]\cdot\boldsymbol{S}_0^\alpha \tag{22}$$

where, $\alpha,\beta\in\mathcal{PA}$.

A system of equations is obtained of the following form,

$$\sum_{\beta\in\mathcal{PA}}A^{\alpha\beta}\Delta\gamma^\beta=b^\alpha \tag{23}$$

where,

$$\begin{aligned}A^{\alpha\beta}&=h^{\alpha\beta}+\frac{1}{2}sign(\boldsymbol{\tau}^\alpha_{trial})sign(\boldsymbol{\tau}^\beta_{trial})\mathcal{L}^e\left[\boldsymbol{B}^\beta\right]\cdot\boldsymbol{S}_0^\alpha\\ b^\alpha&=|\tau^\alpha_{trial}|-s^\alpha\end{aligned} \tag{24}$$

If for any system $\Delta\gamma^\beta\leqslant 0$, then this system is removed from the set of potentially active systems. The system is repeatedly solved until for all systems $\Delta\gamma^\beta>0$.

A.2. Implicit computation of tangent moduli

The linearization process of PK-I stress is given by:

$$\delta\boldsymbol{P}=\delta((\det\boldsymbol{F})\boldsymbol{\sigma}\boldsymbol{F}^{-T})=\det\boldsymbol{F}\left(\mathrm{tr}(\delta\boldsymbol{F}\boldsymbol{F}^{-1})\boldsymbol{\sigma}-\boldsymbol{\sigma}(\delta\boldsymbol{F}\boldsymbol{F}^{-1})^T+\delta\boldsymbol{\sigma}\right)\boldsymbol{F}^{-T} \tag{25}$$

$\delta\boldsymbol{\sigma}$ can be expressed as:

$$\delta\boldsymbol{\sigma}=\delta\left(\frac{1}{\det\boldsymbol{F}^e}\boldsymbol{F}^e\bar{\boldsymbol{T}}(\boldsymbol{F}^e)^T\right) \tag{26}$$

The above expression requires the evaluation of $\delta\boldsymbol{F}^e$ and $\delta\bar{\boldsymbol{T}}$ using the constitutive model. In order to obtain $\delta\bar{\boldsymbol{T}}$, we consider the linearization of Eq. (21) to obtain:

$$\begin{aligned}\delta\bar{\boldsymbol{T}}=&\mathcal{L}^e[\delta\bar{\boldsymbol{E}}^e_{trial}]-\frac{1}{2}\sum_\beta \mathrm{sgn}(\tau^\beta_{trial})\delta(\Delta\gamma^\beta)\mathcal{L}^e\left[\boldsymbol{B}^\beta\right]\\ &-\sum_\beta \mathrm{sgn}(\tau^\beta_{trial})\Delta\gamma^\beta\mathcal{L}^e\left[\boldsymbol{S}_0^{\beta^T}\delta\bar{\boldsymbol{E}}^e_{trial}+\delta\bar{\boldsymbol{E}}^e_{trial}\boldsymbol{S}_0^\beta\right]\end{aligned} \tag{27}$$

This computation of $\delta\bar{\boldsymbol{T}}$ requires the evaluation of $\delta(\Delta\gamma^\beta)$, obtained by linearization given by:

$$\delta(\Delta\gamma^\beta)=(A^{\alpha\beta})^{-1}(\delta b^\alpha-\delta A^{\alpha\beta}\Delta\gamma^\beta) \tag{28}$$

$$\delta b^\alpha=\mathrm{sgn}(\tau^\alpha_{trial})\mathcal{L}^e[\delta\bar{\boldsymbol{E}}^e_{trial}]\cdot\boldsymbol{S}_0^\alpha \tag{29}$$

$$\delta A^{\alpha\beta}=\mathrm{sgn}(\tau^\alpha_{trial})\mathrm{sgn}(\tau^\beta_{trial})\boldsymbol{S}_0^\alpha\cdot\mathcal{L}^e\left[\boldsymbol{S}_0^{\beta^T}\delta\bar{\boldsymbol{E}}^e_{trial}+\delta\bar{\boldsymbol{E}}^e_{trial}\boldsymbol{S}_0^\beta\right] \tag{30}$$

Using the definition of $\delta\bar{\boldsymbol{E}}^e_{trial}=\mathrm{sym}(\boldsymbol{F}^{e^T}_{trial}\delta\boldsymbol{F}\boldsymbol{F}_n^{p^{-1}})$, the above set of equation yield an implicit form $\delta(\Delta\gamma^\beta)=\boldsymbol{m}^\beta\cdot\delta\boldsymbol{F}$ for use in Eq. (27). Next, $\delta\boldsymbol{F}^e$ is obtained from:

$$\delta(\boldsymbol{F}^e)=\delta\boldsymbol{F}(\boldsymbol{F}^p)^{-1}-\boldsymbol{F}^e_{trial}\sum_\beta \mathrm{sgn}(\tau^\beta_{trial})\delta(\Delta\gamma^\beta)\boldsymbol{S}_0^\beta \tag{31}$$

References

Agwai, A., Guven, I., Madenci, E., 2011. Predicting crack propagation with peridynamics: a comparative study. Int. J. Fract. 171, 65–78. http://dx.doi.org/10.1007/s10704-011-9628-4 <http://dx.doi.org/10.1007/s10704-011-9628-4>.

Allison, J., Backman, D., Christodoulou, L., 2006. Integrated computational materials engineering: a new paradigm for the global materials profession. J. Miner. Metals Mater. Soc. 58, 25–27. http://dx.doi.org/10.1007/s11837-006-0223-5.

Anand, L., Kalidindi, S., 1994. The process of shear band formation in plane strain compression of fcc metals: effects of crystallographic texture. Mech. Mater. 17, 223–243. http://dx.doi.org/10.1016/0167-6636(94)90062-0.

Anand, L., Kothari, M., 1996. A computational procedure for rate-independent crystal plasticity. J. Mech. Phys. Solids 44, 525–558. http://dx.doi.org/10.1016/0022-5096(96)00001-4.

Armero, F., Garikipati, K., 1996. An analysis of strong discontinuities in multiplicative finite strain plasticity and their relation with the numerical simulation of strain localization in solids. Int. J. Solids Struct. 33, 2863–2885. http://dx.doi.org/10.1016/0020-7683(95)00257-X.

Bazant, Z., Belytschko, T., Chang, T., 1984. Continuum theory for strain softening. J. Eng. Mech 110, 1666–1692. http://dx.doi.org/10.1061/(ASCE)0733-9399(1984)110:12(1666).

Beaudoin, A.J., Mecking, H., Kocks, U.F., 1996. Development of localized orientation gradients in fcc polycrystals. Philos. Mag. A 73, 1503–1517. http://dx.doi.org/10.1080/01418619608242998.

Becker, R., Panchanadeeswaran, S., 1995. Effects of grain interactions on deformation and local texture in polycrystals. Acta Metall. Mater 43, 2701–2719. http://dx.doi.org/10.1016/0956-7151(94)00460-Y.

Breitenfeld, M., Geubelle, P., Weckner, O., Silling, S., 2014. Non-ordinary state-based peridynamic analysis of stationary crack problems. Comput. Methods Appl. Mech. Eng. 272, 233–250, URL <http://www.sciencedirect.com/science/article/pii/S0045782514000073>, http://dx.doi.org/10.1016/j.cma.2014.01.002.

Bronkhorst, C.A., Kalidindi, S.R., Anand, L., 1992. Polycrystalline plasticity and the evolution of crystallographic texture in fcc metals. Philos. Trans. R. Soc. London A 341, 443–477. http://dx.doi.org/10.1098/rsta.1992.0111.

Coleman, B.D., Hodgdon, M.L., 1987. On shear bands in ductile materials. In: Analysis and Thermomechanics. Springer, Berlin Heidelberg, pp. 227–255. http://dx.doi.org/10.1007/978-3-642-61598-6-14.

Dmitrieva, O., Dondl, P.W., Mller, S., Raabe, D., 2009. Lamination microstructure in shear deformed copper single crystals. Acta Mater. 57, 3439–3449. http://dx.doi.org/10.1016/j.actamat.2009.03.035.

Ghosh, S., Kumar, A., Sundararaghavan, V., Waas, A.M., 2013. Non-local modeling of epoxy using an atomistically-informed kernel. Int. J. Solids Struct. 50, 2837–2845. http://dx.doi.org/10.1016/j.ijsolstr.2013.04.025.

Ghosh, S., Sundararaghavan, V., Waas, A.M., 2014. Construction of multi-dimensional isotropic kernels for nonlocal elasticity based on phonon dispersion data. Int. J. Solids Struct. 51, 392–401. http://dx.doi.org/10.1016/j.ijsolstr.2013.10.004.

Harren, S., Asaro, R., 1989. Nonuniform deformations in polycrystals and aspects of the validity of the taylor model. J. Mech. Phys. Solids 37, 191–232. http://dx.doi.org/10.1016/0022-5096(89)90010-0.

Harren, S., Dve, H., Asaro, R., 1988. Shear band formation in plane strain compression. Acta Metall. 36, 2435–2480. http://dx.doi.org/10.1016/0001-6160(88)90193-9.

Ising, E., 1925. Beitrag zur theorie des ferromagnetismus. Z. Phys. 31, 253–258.

Kammers, A., Daly, S., 2013. Digital image correlation under scanning electron microscopy: methodology and validation. Exp. Mech. 53, 1743–1761. http://dx.doi.org/10.1007/s11340-013-9782-x, URL <http://dx.doi.org/10.1007/s11340-013-9782-x>.

Oliver, J., 1989. A consistent characteristic length for smeared cracking models. Int. J. Numer. Methods Eng. 28, 461–474. http://dx.doi.org/10.1002/nme.1620280214.

Qidwai, M.S., Lewis, A.C., Geltmacher, A.B., 2009. Using image-based computational modeling to study microstructure yield correlations in metals. Acta Mater. 57, 4233–4247. http://dx.doi.org/10.1016/j.actamat.2009.05.021.

Samaniego, E., Belytschko, T., 2005. Continuum discontinuum modelling of shear bands. Int. J. Numer. Methods Eng. 62, 1857–1872. http://dx.doi.org/10.1002/nme.1256.

Sarma, G., Radhakrishnan, B., Dawson, P., 2002. Mesoscale modeling of microstructure and texture evolution during deformation processing of metals. Adv. Eng. Mater. 4, 509–514.

Silling, S., 2000. Reformulation of elasticity theory for discontinuities and long-range forces. J. Mech. Phys. Solids 48, 175–209. http://dx.doi.org/10.1016/S0022-5096(99)00029-0.

Silling, S., Epton, M., Weckner, O., Xu, J., Askari, E., 2007. Peridynamic states and constitutive modeling. J. Elast. 88, 151–184. http://dx.doi.org/10.1007/s10659-007-9125-1.

Sun, S., Sundararaghavan, V., 2012. A probabilistic crystal plasticity model for modeling grain shape effects based on slip geometry. Acta Mater. 60, 5233–5244. http://dx.doi.org/10.1016/j.actamat.2012.05.039.

Sundararaghavan, V., Waas, A., 2011. Non-local continuum modeling of carbon nanotubes: physical interpretation of non-local kernels using atomistic simulations. J. Mech. Phys. Solids 59, 1191–1203. http://dx.doi.org/10.1016/j.jmps.2011.03.009.

Sundararaghavan, V., Zabaras, N., 2006. Design of microstructure-sensitive properties in elasto-viscoplastic polycrystals using multi-scale homogenization. Int. J. Plast. 22, 1799–1824. http://dx.doi.org/10.1016/j.ijplas.2006.01.001.

Sundararaghavan, V., Zabaras, N., 2008. A multi-length scale sensitivity analysis for the control of texture-dependent properties in deformation processing. Int. J. Plast. 24, 1581–1605. http://dx.doi.org/10.1016/j.ijplas.2007.12.005.

Warren, T.L., Silling, S.A., Askari, A., Weckner, O., Epton, M.A., Xu, J., 2009. A non-ordinary state-based peridynamic method to model solid material deformation and fracture. Int. J. Solids Struct. 46, 1186–1195. http://dx.doi.org/10.1016/j.ijsolstr.2008.10.029.

Zhu, R., Zhou, J., Jiang, H., Zhang, D., 2012. Evolution of shear banding in fully dense nanocrystalline ni sheet. Mech. Mater. 51, 29–42. http://dx.doi.org/10.1016/j.mechmat.2012.01.008.